



## Three-dimensional morphological measurements of $\text{LiCoO}_2$ and $\text{LiCoO}_2/\text{Li}(\text{Ni}_{1/3}\text{Mn}_{1/3}\text{Co}_{1/3})\text{O}_2$ lithium-ion battery cathodes

Zhao Liu<sup>a,\*</sup>, J. Scott Cronin<sup>a</sup>, Yu-chen K. Chen-Wiegar<sup>b</sup>, James R. Wilson<sup>a</sup>, Kyle J. Yakal-Kremiski<sup>a</sup>, Jun Wang<sup>b</sup>, Katherine T. Faber<sup>a</sup>, Scott A. Barnett<sup>a</sup>

<sup>a</sup> Department of Materials Science and Engineering, Northwestern University, 2220 Campus Drive, Evanston, IL 60208, USA

<sup>b</sup> Photon Science Directorate, Brookhaven National Laboratory, 75 Brookhaven Avenue, Bldg 725D, Upton, NY 11973, USA

### HIGHLIGHTS

- ▶ 3D morphologies of  $\text{LiCoO}_2$  and  $\text{LiCoO}_2/\text{Li}(\text{Ni}_{1/3}\text{Mn}_{1/3}\text{Co}_{1/3})\text{O}_2$  cathodes were evaluated.
- ▶ FIB-SEM and transmission X-ray microscopy (TXM) tomographic methods were compared.
- ▶ Statistical analyses were done on multiple image volumes to assess data accuracy.
- ▶ Spatial and cell-to-cell microstructure variations were found in cathodes.
- ▶ Transition metal elements found on anode may explain the capacity fade.

### ARTICLE INFO

#### Article history:

Received 24 September 2012

Received in revised form

14 November 2012

Accepted 15 November 2012

Available online 23 November 2012

#### Keywords:

Lithium-ion battery

Tomography

Microstructure

Statistical analysis

### ABSTRACT

The three-dimensional (3D) morphologies of two types of lithium-ion battery cathodes,  $\text{LiCoO}_2$  (LCO) and  $\text{LiCoO}_2/\text{Li}(\text{Ni}_{1/3}\text{Mn}_{1/3}\text{Co}_{1/3})\text{O}_2$  (LCO/NMC) composites, have been measured using focused ion beam – scanning electron microscopy (FIB-SEM) and transmission X-ray microscopy (TXM). TXM measurements were taken at X-ray energies that can provide clear contrast between LCO and NMC particles in the composite cathodes. Multiple three-dimensional image volumes were collected and statistical analyses were done to assess the accuracy and spatial variation of structural parameters including oxide volume fractions, surface areas, and particle size distributions. Comparisons of un-cycled and cycled batteries showed small changes in structure, but spatial and cell-to-cell microstructural variations, found especially in the LCO/NMC cathodes, were large enough to limit the ability to distinguish actual cycling-induced structure changes. The observation of cathode metal cations on the battery anode after cycling may explain, at least in part, the observed ~30% capacity loss.

© 2012 Elsevier B.V. All rights reserved.

### 1. Introduction

Although lithium-ion batteries (LIBs) are highly developed and commercialized [1], increasing battery energy capacity, power density, and cycle life are critical problems for newer applications such as transportation and large-scale grid storage. These issues are being addressed via a number of approaches, especially with new cathode compositions [2]. One less studied aspect that has the potential to provide insight into LIB capacity loss is the 3D electrode morphology. For example, accurate 3D simulations of electrode lithiation and de-lithiation, based on measured 3D morphology, show local details of the lithiation/de-lithiation process [3,4]. This

knowledge can help to reduce cycling-induced degradation by showing how to avoid locally extreme potentials during high power (high C-rate) operation and minimize electrode microstructural changes such as cracking and active material dissolution [5–10].

The rapid development of three-dimensional (3D) microscopy tomography techniques offers an effective route to quantitative assessment of materials with complex structures [11]. Tomography enables the quantification of a number of important geometric parameters, such as volume fraction, surface area, contiguity, tortuosity, and particle size distribution [12–14]. These parameters are believed to affect LIB performance and are necessary for precise LIB modeling. Recently, several studies have been reported to show 3D tomographic data for characterizing LIB electrodes [15–20]. By applying focused ion beam-scanning electron microscopy (FIB-SEM) in LIB electrodes, 3D microstructures of  $\text{LiCoO}_2$  and  $\text{LiFePO}_4$  cathodes were reconstructed and quantified [15–17]. X-ray

\* Corresponding author. Tel.: +1 847 491 5949; fax: +1 847 491 7820.

E-mail address: [zhaoliu2015@u.northwestern.edu](mailto:zhaoliu2015@u.northwestern.edu) (Z. Liu).

computed tomography characterization of a LIB graphite anode and of the structural evolution of  $\text{LiVO}_2$  electrodes due to oxidation have also been reported [18–20]. To date, only two full 3D simulations of electrode cycling, based on a  $\text{LiCoO}_2$  3D microstructure, have been reported [3,4]. Thus, the correlation of morphology with battery performance and cycling characteristics is still mostly unexplored for other electrode chemistries. Furthermore, the statistical significance and representativeness of measured 3D volumes have not yet been addressed.

The present work was undertaken with two related goals in mind. The first was to obtain extensive data for two important commercial LIB cathodes,  $\text{LiCoO}_2$  (LCO) and  $\text{LiCoO}_2/\text{Li}(\text{Ni}_{1/3}\text{Mn}_{1/3}\text{Co}_{1/3})\text{O}_2$  (LCO/NMC), enough to fully assess the statistical accuracy of the data. The second was to investigate the applicability of 3D tomography for studying LIB electrode microstructure evolution on electrochemical cycling. Because the measurements involve disassembly of the battery, it was necessary to compare electrodes from two different, but nearly identical, batteries—one after cycling and the other in the un-cycled state. Thus, statistical accuracy, spatial variations, and battery-to-battery variations must be known in order to assess the validity of observed microstructural changes. The LCO and LCO/NMC cathodes, both from cycled and un-cycled batteries, were reconstructed using data from both FIB-SEM and full-field transmission X-ray microscopy (TXM). The advantages and limitations of these techniques are also discussed. Finally, energy dispersive X-ray spectroscopy (EDS) analysis of the anodes was used to assist in the understanding of LIB degradation.

## 2. Experimental methods

Four commercial 18650 cells (Lishen, Tianjin, China) with two types of cathode active materials – fresh and cycled cells with either LCO or LCO/NMC cathodes – were investigated in this report. The fresh cells were fully discharged once and the cycled cells were electrochemically cycled between 2.5 V and 4.6 V for several hundred cycles. The LCO cell exhibited a 20% capacity loss after cycling, while the LCO/NMC cell lost 30% of its initial capacity. All cells were then opened in their fully discharged state and the electrolyte evaporated. In order to limit any damage to the sample during preparation, all cathode samples were gently cut with a razor blade from the electrode without washing.

### 2.1. FIB-SEM tomography

Eight sample pieces (four from LCO cathodes and four from LCO/NMC cathodes) were cut from different locations on the cathodes for imaging with FIB-SEM serial sectioning. A commercial low viscosity epoxy (Epo-Thin, Buehler, Illinois, USA) was vacuum infiltrated into these samples to fill the porosity and enhance the contrast for SEM imaging. During the infiltration process, the pressure was kept as low as 50 mbar to improve infiltration. After the epoxy cured, all samples were polished with SiC paper down to 1200 grit to obtain a smooth top surface for FIB milling. Finally, either osmium or gold was sputtered on these samples to prevent charging during FIB-SEM data collection.

All samples were serial-sectioned using either a Zeiss NVision 40 dual beam FIB-SEM or an FEI Helios FIB-SEM. The pixel size of the SEM images ranged from 50 nm to 62.5 nm, while the slice thicknesses were either 150 nm or 200 nm. These resolution values were  $<1/10$  of the typical feature sizes in the cathodes, as required to provide acceptably accurate 3D reconstructions [21]. The data sets, comprised of a series of 2D images, were then aligned, segmented, and stacked into 3D reconstructions [22–24]. The image segmentation for each cathode is described in detail later. Eight 3D reconstructions with volumes ranging from  $\sim 28,000$

**Table 1**

Microstructural parameters calculated from LCO cathode 3D reconstructed data sets.

Microstructural parameter	Samples			
	Fresh 1	Fresh 2	Fresh 3	Cycled
Total Volume ( $\mu\text{m}^3$ )	28,123	44,331	37,423	42,395
LCO $V_f$ (%)	68.4	69.1	66.3	69.5
(Pore + other) $V_f$ (%)	31.6	30.9	33.7	30.5
LCO $\text{SA}_f$ ( $\mu\text{m}^{-1}$ )	0.62	0.65	0.64	0.67
LCO $\text{SA}_s$ ( $\mu\text{m}^{-1}$ )	0.91	0.94	0.97	0.97

to  $\sim 63,000 \mu\text{m}^3$  were obtained for morphological quantification and statistical analyses. Details for each data set are described in Tables 1 and 2 for LCO and Tables 3 and 4 for LCO/NMC.

### 2.2. X-ray nanotomography

One cycled LCO/NMC cathode sample was studied using full-field transmission X-ray microscopy (TXM) [25]. A cylindrical sample with a diameter of about 35  $\mu\text{m}$  and height of about 60  $\mu\text{m}$  was milled from the LCO/NMC sample using a focused ion beam. The cylindrical sample was then platinum welded onto a sharp tungsten pin using an FIB lift-out technique [25]. Two sequential tomographic data sets were collected to take advantage of the tunability of synchrotron radiation. Incident X-ray energies of either 8200 eV or 7600 eV were chosen to provide phase contrast between LCO and NMC. Each tomographic data set was collected with 1441 projections over the angular range of  $180^\circ$  with a field of view of  $40 \times 40 \mu\text{m}^2$  (the  $2k \times 2k$  CCD camera binned  $2 \times 2$  pixels). A standard filtered back-projection reconstruction algorithm was used to reconstruct the 3D images [26]. The total size of the reconstructed sample volume is a cylinder of about 35  $\mu\text{m}$  in diameter and 40  $\mu\text{m}$  in height, with a voxel size of 38.9 nm. The two reconstructed stacks were registered in 3D space by maximizing the cross-correlation coefficient using Avizo commercial software package (VSG, version 6, Massachusetts, USA) before segmentation.

The segmentation and data analysis was conducted after cropping a central volume of  $\sim 11,000 \mu\text{m}^3$  from the total reconstruction. The images collected at 8200 eV were used to segment the LCO phase with a simple thresholding method based on the well-separated gray scale histogram peak. A similar step was taken to isolate the NMC phase in the 7600 eV data. The remaining volume, including epoxy-filled porosity, non-evaporated electrolyte residue, carbon, and binder, was automatically segmented as one phase by obtaining the intersection of non-LCO phase and non-NMC phases.

### 2.3. Microstructure quantification and statistical analysis

Microstructural parameters, including phase volume fraction ( $V_f$ ), interfacial surface area density ( $\text{SA}_f$ ), and specific surface area density ( $\text{SA}_s$ ) were calculated from the 3D images as described elsewhere [22,23,27].  $\text{SA}_f$  is determined by normalizing the surface

**Table 2**

Statistical analysis results for the LCO phase from 3D reconstructed data sets.

Statistical parameter	Samples		
	Fresh (LCO)	Cycled (LCO)	P-value
Average $V_f$ (%)	68.0	69.5	0.184
Standard error	0.9	1.4	
Average $\text{SA}_f$ ( $\mu\text{m}^{-1}$ )	0.64	0.67	0.09
Standard error ( $\mu\text{m}^{-1}$ )	0.01	0.02	
Average $\text{SA}_s$ ( $\mu\text{m}^{-1}$ )	0.94	0.97	0.145
Standard error ( $\mu\text{m}^{-1}$ )	0.02	0.02	

**Table 3**

Microstructural parameters calculated from the 3D reconstructed LCO/NMC cathodes.

Microstructural parameter	Samples			
	Fresh 1	Fresh 2	Cycled 1	Cycled 2
Total volume ( $\mu\text{m}^3$ )	52,249	62,851	41,703	62,637
LCO $V_f$ (%)	34.0	25.0	42.8	38.6
NMC $V_f$ (%)	32.1	38.7	25.0	30.7
LCO $SA_i$ ( $\mu\text{m}^{-1}$ )	0.30	0.25	0.38	0.33
NMC $SA_i$ ( $\mu\text{m}^{-1}$ )	0.59	0.57	0.53	0.50
LCO $SA_s$ ( $\mu\text{m}^{-1}$ )	0.88	1.00	0.89	0.85
NMC $SA_s$ ( $\mu\text{m}^{-1}$ )	1.84	1.47	2.12	1.63

area of each phase by the total reconstruction volume, while  $SA_s$  is established by normalizing the surface area of each phase by the volume of that phase. A normalized continuous particle size distribution (continuous PSD<sub>C</sub>) is calculated for all cathode reconstructions using the method developed by Münch and Holzer [28], as the calendaring process and the use of a binder during the electrode fabrication produces a complex interconnected microstructure in the cathode. Particle size distribution (PSD) of the analyzed volume is calculated as the derivative of the continuous PSD<sub>C</sub>.

In order to evaluate any microstructural changes on cycling, a statistical analysis method – namely one-stage cluster sampling with equal probabilities – was used in the current study [29]. One can consider the electrode being comprised of  $N$  clusters of voxel elements. Of these  $N$  clusters, a small subset of  $n$  clusters is selected for reconstruction, each containing  $M_i$  voxel elements. A quantity of interest ( $t_i$ ), e.g. phase volume and surface area, in each cluster  $i$  can be calculated by simply summing the contribution from each voxel element:

$$t_i = \sum_{j=1}^{M_i} x_{ij} \quad (1)$$

where  $x_{ij}$  is the measurement of the  $j$ th element in the  $i$ th cluster. Microstructural parameters calculated this way are extrinsic, and are expected to be positively correlated with  $M_i$ . Hence, the ratio estimator is calculated to provide a normalized, intrinsic value, such as the phase volume fraction and interfacial or specific surface area. The mean ratio estimator is

$$\hat{y}_r = \frac{\sum_{i \in S} t_i}{\sum_{i \in S} M_i} \quad (2)$$

and the standard error estimator is

$$SE(\hat{y}_r) = \sqrt{\left(1 - \frac{n}{N}\right) \frac{1}{n\bar{M}_S^2} \frac{\sum_{i \in S} M_i^2 (\bar{y}_i - \hat{y}_r)^2}{n-1}} \quad (3)$$

where  $S$  designates all the chosen clusters from the electrode,  $\bar{M}_S$  is the average number of elements of all the chosen clusters and  $\bar{y}_i$  is

sample mean of the cluster  $i$ . As the volume of the electrode is much larger than the volume of clusters,  $N \gg n$ ,  $\left(1 - \frac{n}{N}\right) \approx 1$ , Eq. (3) can be simplified to

$$SE(\hat{y}_r) \approx \sqrt{\frac{1}{n\bar{M}_S^2} \frac{\sum_{i \in S} M_i^2 (\bar{y}_i - \hat{y}_r)^2}{n-1}} \quad (4)$$

From the mean ratio estimator and the standard error estimator, any microstructural parameter changes upon cycling can be evaluated by running a statistical Z-test [30]. A one-tailed Z-test was conducted with the null hypothesis that the microstructural parameters are the same between the fresh and cycled cathodes. The alternative hypothesis was that the microstructural parameters in the cycled cathode are larger or smaller than the fresh cathode. The Z-value is calculated and the  $P$ -value, the probability that the samples are statistically identical, is then obtained based on the Z-value and is used to decide whether to reject the null hypothesis so as to evaluate the significance of any microstructural changes.

## 2.4. EDS analysis

Energy dispersive X-ray spectroscopy (EDS) mapping was performed on the LCO/NMC cathode to assist the segmentation of LCO and NMC particles. The cross-section used for EDS data collection was obtained by FIB cleaning the wall of the rectangular trench that was formed after FIB-SEM data set collection. The cleaning process was performed in the FEI Helios FIB-SEM and data were collected using the Integrated Oxford EDS system. In order to probe the possibility of active material dissolution and migration of transition metal ions during cycling, two samples were cut from the graphite anodes of the two LCO and LCO/NMC opened cycled cells. Both samples were washed with dimethyl carbonate (DMC) and dried before EDS analysis on the Hitachi S-3400N-II.

## 3. Results and discussion

### 3.1. LiCoO<sub>2</sub> cathode

Fig. 1(a) shows a typical 2D cross-section of the cycled LCO cathode data set from SEM imaging. The light gray phase represents the LCO particles, which are irregular in shape with many internal cracks clearly visible. There is little atomic Z-contrast difference among the porosity filled with epoxy resin, carbon black, binder and nonvolatile electrolyte residues as they are all carbon-based organics, and therefore this portion appears uniformly black in the image. This image is similar to that reported previously for fresh LCO cathodes [15]. The good image contrast allows for accurate segmentation of 2D slices via thresholding by the Otsu algorithm [31], after image alignment and cropping has been performed. The 2D binary image shown in Fig. 1(b) is an example of a segmented image ready for 3D reconstruction. Fig. 1(c) and (d) show the 3D reconstruction corresponding to both phases in the cathode.

Three fresh LCO cathode sample volumes were reconstructed. Microstructural quantification was performed on these through the cluster sampling scheme; the results, along with those for the cycled cathode, are compiled in Table 1. The values obtained agree well with those reported previously for this same fresh cathode [15]. Statistical analysis of the estimations of mean and standard error for  $V_f$ ,  $SA_i$ ,  $SA_s$  were obtained and are given in Table 2. Standard deviations ( $= SE(\hat{y}_r) * \sqrt{n}$ ) of  $V_f$ ,  $SA_i$  and  $SA_s$  in fresh LCO cathode samples, found to be 1.5%, 0.02  $\mu\text{m}^{-1}$  and 0.03  $\mu\text{m}^{-1}$ , respectively, were also calculated based on standard error estimations. There are no outliers for all samples in these parameters,

**Table 4**

Statistical analysis results for LCO/NMC cathode from 3D reconstructed data sets.

Microstructural parameter	Samples					
	Fresh LCO	Cycled LCO	$P$ -value	Fresh NMC	Cycled NMC	$P$ -value
Average $SA_s$ ( $\mu\text{m}^{-1}$ )	0.94	0.87		1.62	1.80	
Standard error	0.06	0.02	0.136	0.18	0.22	0.263

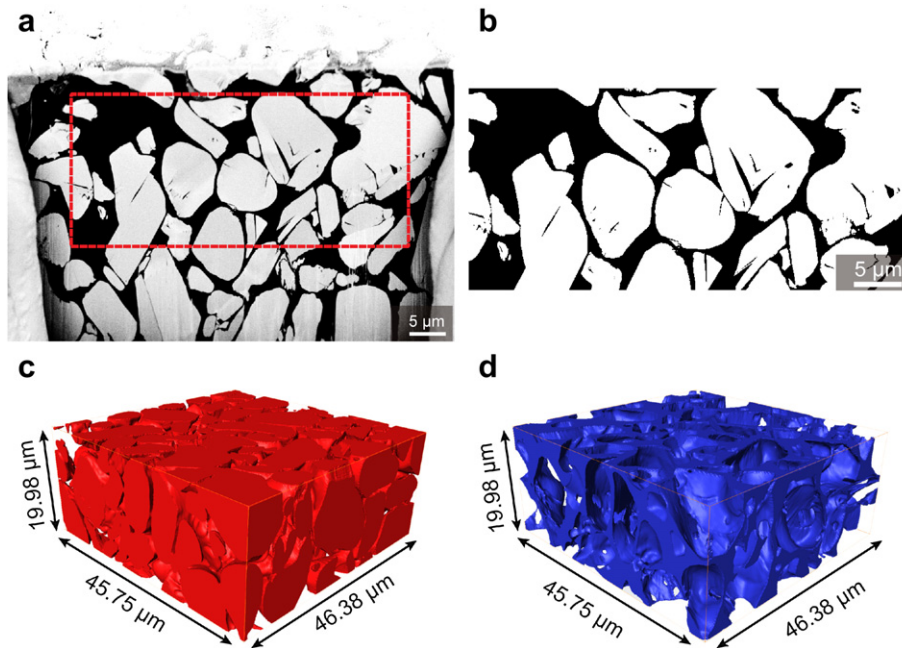


**Fig. 1.** (a) Cross-sectional SEM image of the cycled LCO cathode sample after FIB milling. (b) Segmented image corresponding to the red dashed rectangle region in (a). (c) 3D reconstruction of the cathode LCO phase. (d) 3D reconstruction of the cathode non-oxide phases, i.e., electrolyte space, nonvolatile electrolyte, carbon black, and binder. (For interpretation of the references to color in this figure legend, the reader is referred to the web version of this article.)

which indicate that the reconstruction volumes used in this report are large enough to be representative of the full cathode and that the particles are distributed homogeneously within the cathode.

Because the particles were proven to be distributed homogeneously in the fresh battery and as both batteries are from the same batch, we rely on the cluster sampling scheme of the cycled LCO cathode similar to that used for the fresh LCO cathode, but only one cluster was chosen. In order to estimate the standard error for the cycled sample, a plausible assumption follows that the ratio estimator variances of fresh versus cycled samples are equal.

$$(s_{tf})^2 = \frac{\sum_{i \in S} (t_i - \hat{t})^2}{n-1} = \frac{\sum_{i \in S} M_i^2 (\bar{y}_i - \hat{y}_r)^2}{n-1} = (s_{tc})^2 \quad (5)$$

Here  $\hat{t}$  is the estimator of a microstructural parameter value for the whole electrode, and  $(s_{tf})^2$  and  $(s_{tc})^2$  are the ratio estimator variances of fresh and cycled cathode samples, respectively. The standard error estimator of the cycled sample is given in Table 2. After conducting a Z-test, *P*-values were obtained (Table 2). The statistical results show that none of the microstructural parameters changed significantly after cycling when a 5% significance level is applied, i.e. all three *P*-values are greater than 0.05.

Continuous PSD<sub>C</sub> were calculated to investigate the impact of cycling on particle size. Fig. 2(a) and (b) shows the continuous PSD<sub>C</sub> and PSD of the four reconstructed LCO samples. They appear nearly identical in the small particle diameter range (lower than 4 μm) and show only small differences as particle size increases. These differences at the large diameter range stem from the effects of a few extremely large LCO particles within the reconstruction volume. However, no significant impact on the particle size has been found to occur with cycling. Therefore, under these electrochemical cycling conditions, no microstructural changes, such as particle fracture and change in particle size in the cathode particles, are discernible.

### 3.2. LCO/NMC mixed cathode

Fig. 3(a) shows a typical 2D cross-sectional SEM image from the fresh LCO/NMC cathode. As confirmed by EDS, there are two types of particles, each with a characteristic morphology; the LCO particles are dense particles with smooth edges, while the NMC phase consists of agglomerates of sub-micron particles with rough edges and internal porosity. Because there is little contrast between LCO and NMC, the segmentation of these two solid active materials was performed manually on an image-by-image basis by identifying the different shapes. Images were pre-segmented into two phases (solid active materials and other non-active material phases), after which the LCO particles were located and labeled separately. This process was checked for accuracy by comparing segmented images with EDS maps of several images. Fig. 3 (b) and (c) demonstrates the good agreement between the segmented image and the EDS mapping of the same region. A 3D image of the reconstructed volume of the fresh LCO/NMC cathode is shown in Fig. 3(d).

TXM nanotomography allows for near-edge differential-absorption imaging to enhance contrast [20,32], in this case between LCO and NMC particles. A detailed study of the application of this technique to investigate LCO/NMC mixed cathodes will be reported elsewhere [33]. Fig. 4(a) shows the reconstructed slice at 8200 eV, where the light gray phase is LCO, the dark gray phase is NMC, and the black phase represents the non-oxide cathode components. The grayscale histogram of a typical image slice shows three well-separated peaks, allowing automatic segmentation of the three phases (Fig. 4(b)).

Four LCO/NMC sample volumes (two fresh, two cycled) were measured via FIB-SEM and 3D morphological quantification was performed. The results are shown in Table 3. The variability of the LCO and NMC volume fractions is large not only between the samples with different cycling conditions, but also between samples from the same cathode at different locations. That is, the electrodes exhibited substantial cell-to-cell variations and spatial variations within cells. Thus, no conclusion can be reached



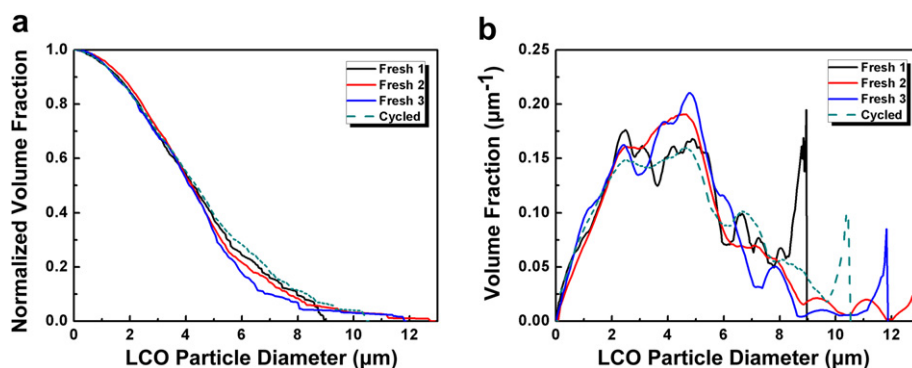


Fig. 2. Continuous particle size distribution (a) and particle size distribution (b) of LCO particles in four samples.

regarding the effect of cycling, because the apparent changes in LCO and NMC volume fractions after cycling can be explained by the electrode variability. Of course, there may be actual changes that were too small to resolve from the electrode variability. One possible mechanism, the dissolution of NMC and its re-deposition on LCO particles surfaces, was ruled out by SEM-EDS analyses of the cycled sample that showed no evidence of Ni or Mn on LCO particle surfaces. The mole fractions of both oxide phases were also calculated based on the volume fraction. The calculations show that the mole fraction of LCO ranges between 39.1% and 62.8% and the mole fraction of NMC is from 37.2% to 60.9%.

The results of surface area calculations are also given in Table 3. The interfacial surface area ( $SA_i$ ) of NMC is larger than LCO, which should help facilitate electrode/electrolyte ion transfer. The specific surface area ( $SA_s$ ) result demonstrates that NMC particles have smaller average diameter than LCO particles. Because the  $V_f$  and  $SA_i$  differences between the fresh and cycled samples are largely influenced by the composition variance caused by poor mixing, statistical analysis is only meaningful for the  $SA_s$ . Table 4 shows the result – the  $SA_s$  is not influenced by the cycling with a 5% significance level. The large standard error, particularly for NMC, further describes the microstructural inhomogeneity in the analyzed cathode.

Morphological quantification was also performed on TXM data and used to compare  $SA_s$  from both TXM and FIB-SEM techniques. Because the reconstruction volume of the FIB-SEM sample is larger than that from the X-ray nanotomography sample, one of the FIB-SEM sample (cycled sample #1) was equally split into 4 sub volumes so that the volume size of data set could be compared to X-ray nanotomography data. As can be seen in Table 5, the NMC phase is comparable to the FIB-SEM result, namely TXM result are within one standard deviation of FIB-SEM result, whereas the LCO phase is not. At this scale, the reconstruction volume size is not large enough to be volumetrically independent, which yields the disagreement with LCO phase fractions.

In order to further interpret the surface area results, continuous PSD<sub>C</sub> and PSD of FIB-SEM data were determined. Fig. 5(a) and (b) shows the normalized continuous PSD<sub>C</sub> and PSD of LCO for fresh and cycled cathodes, respectively. Although there are differences among the samples, no significant PSD changes between fresh and cycled samples are found. Fig. 5(c) and (d) shows the continuous PSD<sub>C</sub> and PSD for the NMC particles, respectively. This result, in which one sample, referred to as fresh #2, has the largest median particle size and another sample referred as cycled #1 has the smallest, agrees well with the  $SA_s$  calculation. Although the PSDs of

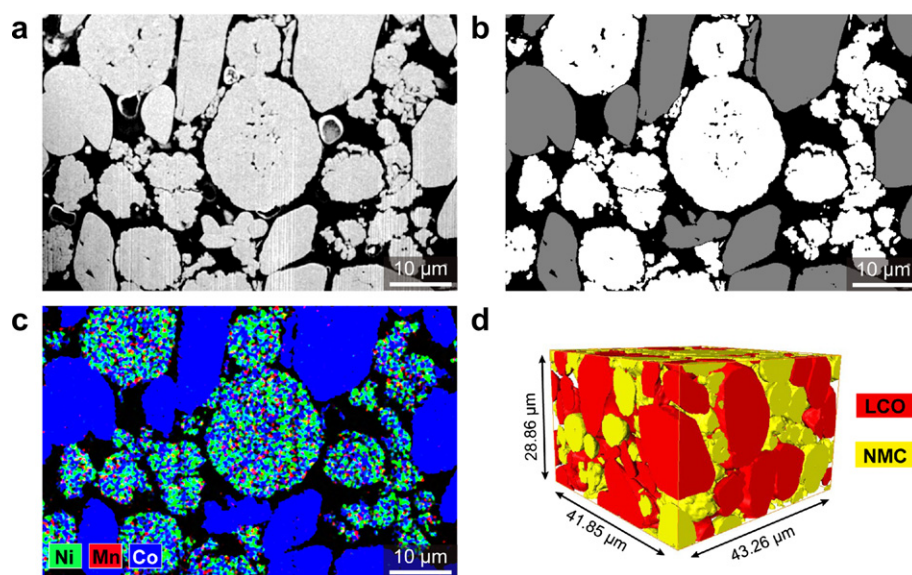
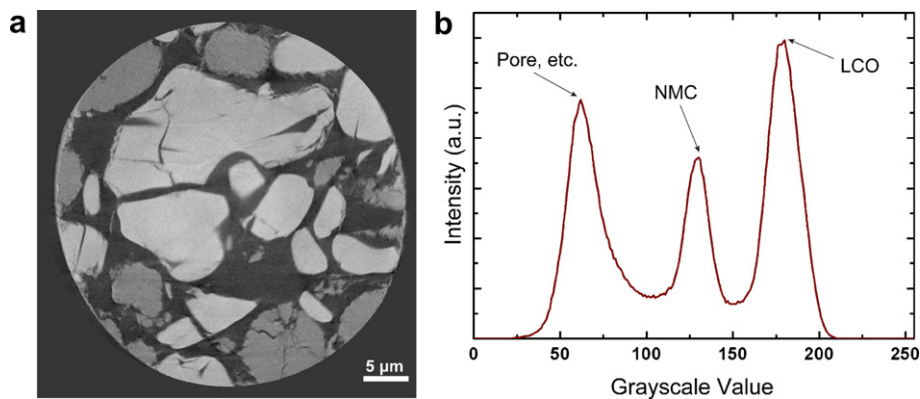


Fig. 3. (a) A cross-sectional SEM image of the fresh LCO/NMC cathode. (b) Corresponding image after segmentation, where white represents NMC, gray represents LCO, black represents epoxy filled pores, carbon black, binder, and nonvolatile electrolyte. (c) EDS mapping of the same position in (a). (d) The 3D reconstruction, where materials except for LCO and NMC are appear transparent.



**Fig. 4.** (a) TXM reconstructed data of a cycled LCO/NMC cathode showing LCO particles (light grey), NMC particles (medium grey), and the electrolyte/binder/carbon volume (dark grey). (b) Gray scale histogram of the reconstructed region in (a).

**Table 5**  
Comparison of  $SA_s$  from FIB-SEM and TXM data.

Microstructural parameter	Samples			
	Cycled LCO (FIB-SEM)	Cycled LCO (TXM)	Cycled NMC (FIB-SEM)	Cycled NMC (TXM)
Average $SA_s$ ( $\mu\text{m}^{-1}$ )	0.89	1.17	2.10	2.13
Standard deviation	0.19		0.18	

NMC in the four samples are different, no significant trend can be found among fresh and cycled samples.

To assess what microstructural changes that would be necessary to observe a statistically significant change in  $SA_s$ , it is estimated that, for the microstructures studied here, at least ~20% of LCO particles and ~50% NMC particles, if cracked into two equal-sized particles, would produce a significant change. This result indicates

that inhomogeneity limits the ability to detect small microstructural changes. Hence, it is expected that a more homogeneous electrode structure is needed to study LIB microstructural evolution via a destructive 3D tomography method like FIB-SEM. On the other hand, the non-destructive TXM method offers the possibility to further investigate inhomogeneous electrodes by exploring the continuous microstructural evolution on the same sample volume before and after cycling [20]. Note that homogeneity itself may be of interest, as recent research shows that electrode material inhomogeneity may have a negative impact on battery performance and may even contribute to degradation [19].

### 3.3. EDS analysis

Previous research suggests that active material dissolution and the deposition of dissolved metal ions on the anode as two possible degradation mechanisms, which could be correlated to capacity

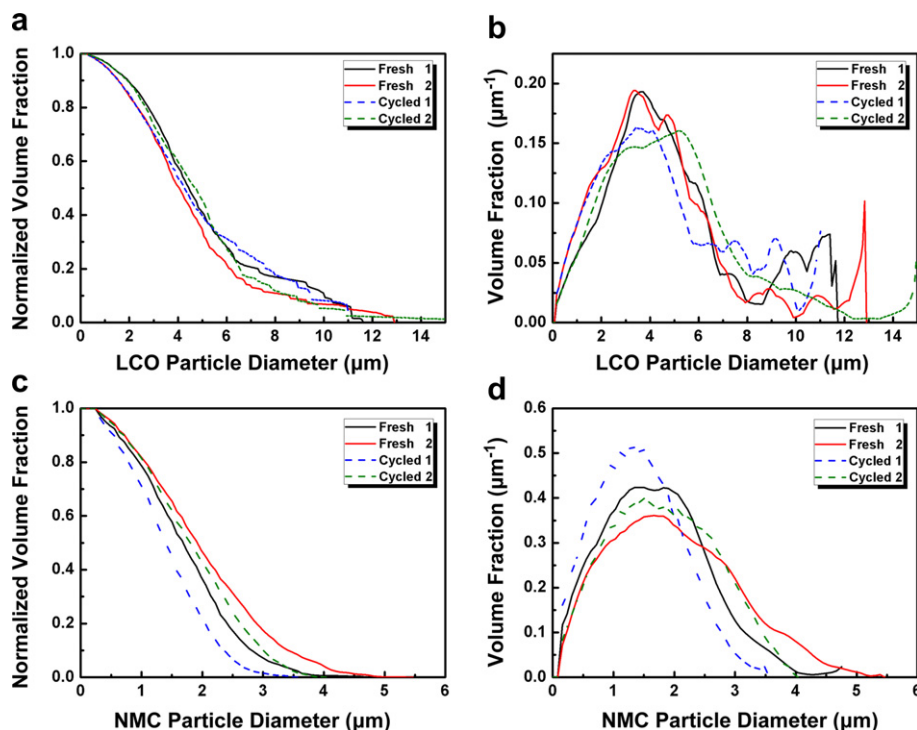


**Fig. 5.** (a) Continuous particle size distribution of LCO particles. (b) Particle size distribution of LCO particles. (c). Continuous particle size distribution of NMC particles. (d) Particle size distribution of NMC particles.

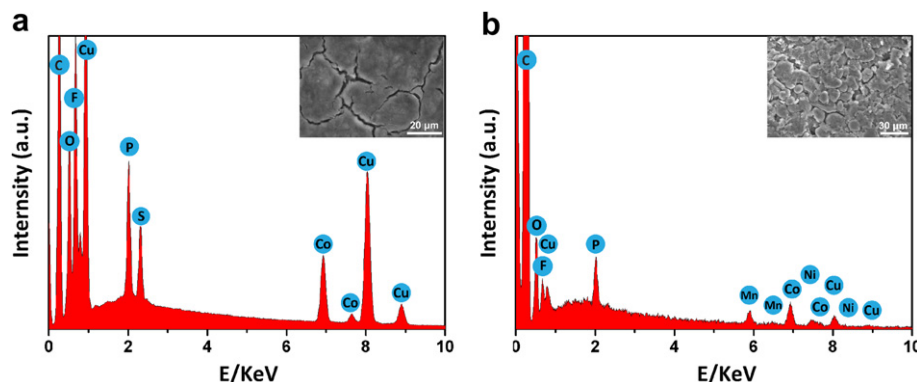


Fig. 6. EDS analyses result of harvested graphite anode of both cycled cells. (a) LCO. (b) LCO/NMC. Insets are the SEM image corresponding to the data collection region.

fade when the cell is cycled with high charge limit [5,9]. Because the cells investigated in the current study were cycled at high operating voltage, EDS was performed on the harvested graphite anodes of both cycled cells to probe the possibility of the contribution of these two mechanisms. Fig. 6 shows the elemental analysis results of anodes cycled against LCO (Fig. 6(a)) and LCO/NMC (Fig. 6(b)) cathodes. The insets are the SEM images of the corresponding region over which the EDS data were collected. The main elements found in these cycled anodes are C, from graphite, O, from organics, P and F, from Li salt ( $\text{LiPF}_6$ ), and Cu, from the current collector. Transition metal ions were also detected on both anodes, which indicates dissolution of the active materials and metal ion deposition during cycling. Very little metal ion deposition is needed to dramatically increase the impedance of the anode, and thus, influence the electrochemical performance of the whole cell [9]. It is hypothesized that this mechanism is correlated to capacity fade of the cycled cell investigated in current study. Such small chemical changes are expected to have minimal influence on the cathode microstructure – particle sizes may change by only a few nanometers [5]. As a result, it is difficult to resolve the microstructural changes by FIB-SEM tomography, especially given the inhomogeneity issues noted above.

#### 4. Conclusions

Two types of commercial LIB cathodes, LCO and LCO/NMC, were studied before and after electrochemical cycling using three-dimensional FIB-SEM tomography. The LCO/NMC cathodes were also analyzed using TXM-based nanotomography, yielding results that mostly agree with the FIB-SEM results. The tomography data were statistically analyzed via cluster sampling. For the LCO cathode, none of the microstructural parameters analyzed were found to change significantly after cycling, even though there was a resulting capacity loss of  $\sim 20\%$ . In the case of LCO/NMC, where cycling caused a  $\sim 30\%$  capacity fade, microstructural inhomogeneities in the analyzed reconstructed volumes limited the ability to statistically distinguish microstructural changes. Deposited metal ions were found on the anode of both cycled cells via EDS analysis. The deposition of these metal ions will increase the impedance of the anode and are probably a partial cause of the observed battery degradation.

Finally, it should be noted that both FIB-SEM and TXM are useful techniques to quantitatively characterize LIB electrode microstructure. When studying inhomogeneous electrodes, such as those in the present commercial batteries, TXM has the advantage of being non-destructive, potentially allowing measurements of the same volume before and after cycling. For LIB electrodes with demonstrably well-controlled, homogeneous, and reproducible

microstructure, comparison of electrode structure from different positions and different batteries may be meaningful, such that the combination of FIB-SEM and statistical analysis methods is suitable. Both methods offer opportunities to probe the microstructural complexity of LIB electrodes and facilitate the use of computational models based on the 3D electrode microstructure.

#### Acknowledgment

The authors acknowledge the financial support from the National Science Foundation Ceramics program (DMR-0907639), the MRSEC program (DMR-1121262) of Northwestern University and Office of Naval Research Grant #N00014-12-1-0713. We thank Dr. Stephen J. Harris for providing battery samples studied in this report, Mr. Jiangtao Gou (Department of Statistics Northwestern Univ.) for useful suggestions in statistics, Mr. Benjamin Myer (Northwestern Univ.) and Dr. Fernando Camino (BNL) for assisting SEM imaging and the development of the sample preparation procedure using FIB-SEM. The FIB-SEM (Zeiss) was accomplished at the Electron Microscopy Center for Materials Research at Argonne National Laboratory under the guidance of Dr. Dean J. Miller and Dr. Jon M. Hiller, a U.S. Department of Energy Office of Science Laboratory operated under Contract No. DE-AC02-06CH11357 by UChicago Argonne, LLC. FIB-SEM (FEI) was performed in the EPIC facility of NUANCE Center at Northwestern University. NUANCE Center is supported by NSF-NSEC, NSF-MRSEC, Keck Foundation, the State of Illinois, and Northwestern University. The X-ray nanotomography and its FIB sample preparation were carried out at Brookhaven National Laboratory, which is supported by the U.S. Department of Energy, Office of Science, Office of Basic Energy Sciences, under Contract No. DE-AC02-98CH10886.

#### References

- [1] B. Dunn, H. Kamath, J.M. Tarascon, *Science* 334 (2011) 928–935.
- [2] J.W. Fergus, *J. Power Sources* 195 (2010) 939–954.
- [3] A.H. Wiedemann, G.M. Goldin, S.A. Barnett, H.Y. Zhu, R.J. Kee, Unpublished results.
- [4] B. Yan, C. Lim, L.L. Yun, L.K. Zhu, *J. Electrochem. Soc.* 159 (2012) A160.
- [5] G.G. Amatucci, J.M. Tarascon, L.C. Klein, *Solid State Ionics* 83 (1996) 167–173.
- [6] H.F. Wang, Y.I. Jang, B.Y. Huang, D.R. Sadoway, Y.T. Chiang, *J. Electrochem. Soc.* 146 (1999) 473–480.
- [7] R. Yazami, Y. Ozawa, H. Gabrisch, B. Fultz, *Electrochim. Acta* 50 (2004) 385–390.
- [8] K. Amine, Z.H. Chen, Z. Zhang, J. Liu, W.Q. Lu, Y. Qin, J. Lu, L. Curtis, Y.K. Sun, *J. Mater. Chem.* 21 (2011) 17754–17759.
- [9] H.H. Zheng, Q.N. Sun, G. Liu, X.Y. Song, V.S. Battaglia, *J. Power Sources* 207 (2012) 134–140.
- [10] J. Vetter, P. Novak, M.R. Wagner, C. Veit, K.C. Moller, J.O. Besenhard, M. Winter, M. Wohlfahrt-Mehrens, C. Vogler, A. Hammouche, *J. Power Sources* 147 (2005) 269–281.
- [11] M.D. Uchic, L. Holzer, B.J. Inkson, E.L. Principe, P. Munroe, *MRS Bull.* 32 (2007) 408–416.

- [12] K.N. Grew, A.A. Peracchio, W.K.S. Chiu, J. Power Sources 195 (2010) 7943–7958.
- [13] K.N. Grew, A.A. Peracchio, A.S. Joshi, J.R. Izzo, W.K.S. Chiu, J. Power Sources 195 (2010) 7930–7942.
- [14] J. Scott Cronin, K. Muangnapoh, Z. Patterson, K.J. Yakal-Kremski, V.P. Dravid, S.A. Barnett, J. Electrochem. Soc. 159 (2012) B385.
- [15] J.R. Wilson, J.S. Cronin, S.A. Barnett, S.J. Harris, J. Power Sources 196 (2011) 3443–3447.
- [16] M. Ender, J. Joos, T. Carraro, E. Ivers-Tiffée, Electrochem. Commun. 13 (2011) 166–168.
- [17] T. Hutzenlaub, S. Thiele, R. Zengerle, C. Ziegler, Electrochem. Solid State 15 (2012) A33–A36.
- [18] V. Yufit, P. Shearing, R.W. Hamilton, P.D. Lee, M. Wu, N.P. Brandon, Electrochem. Commun. 13 (2011) 608–610.
- [19] D. Kehrwald, P.R. Shearing, N.P. Brandon, P.K. Sinha, S.J. Harris, J. Electrochem. Soc. 158 (2011) A1393–A1399.
- [20] Y.C.K. Chen, P. Shearing, Q.X. Yuan, A. Tkachuk, J. Wang, Electrochem. Commun. 21 (2012) 58–61.
- [21] L. Holzer, F. Indutnyi, P.H. Gasser, B. Munch, M. Wegmann, J. Microsc. Oxford 216 (2004) 84–95.
- [22] J.R. Wilson, W. Kobsiriphat, R. Mendoza, H.Y. Chen, J.M. Hiller, D.J. Miller, K. Thornton, P.W. Voorhees, S.B. Adler, S.A. Barnett, Nat. Mater. 5 (2006) 541–544.
- [23] J.R. Wilson, M. Gameiro, K. Mischaikow, W. Kalies, P.W. Voorhees, S.A. Barnett, Microsc. Microanal. 15 (2009) 71–77.
- [24] J.R. Kremer, D.N. Mastronarde, J.R. McIntosh, J. Struct. Biol. 116 (1996) 71–76.
- [25] J. Wang, Y.C.K. Chen, Q.X. Yuan, A. Tkachuk, C. Erdonmez, B. Hornberger, M. Feser, Appl. Phys. Lett. 100 (2012).
- [26] F. Natterer, The Mathematics of Computerized Tomography, first ed., John Wiley & Sons, New York, 1986.
- [27] J.R. Wilson, J.S. Cronin, A.T. Duong, S. Rukes, H.Y. Chen, K. Thornton, D.R. Mumm, S.A. Barnett, J. Power Sources 195 (2010) 1829–1840.
- [28] B. Munch, L. Holzer, J. Am. Ceram. Soc. 91 (2008) 4059–4067.
- [29] S.L. Lohr, Sampling: Design and Analysis, second ed., Duxbury Press, 2009.
- [30] R.C. Sprinthal, Basic Statistical Analysis, ninth ed., Prentice Hall, 2011.
- [31] N. Otsu, IEEE Trans. Syst. Man, Cybernet. 9 (1979) 62–66.
- [32] G.J. Nelson, W.M. Harris, J.J. Lombardo, J.R. Izzo, W.K.S. Chiu, P. Tanasini, M. Cantoni, J. Van Herle, C. Comninellis, J.C. Andrews, Y.J. Liu, P. Pianetta, Y.S. Chu, Electrochem. Commun. 13 (2011) 586–589.
- [33] Y.C.K. Chen, Z. Liu, K.T. Faber, S.A. Barnett, J. Wang, Unpublished results.